



Worm-algorithm-type simulation of the quantum transverse-field Ising model

Chun-Jiong Huang ^{1,2,3}, Longxiang Liu,^{1,2,3} Yi Jiang,^{4,*} and Youjin Deng ^{1,2,3,†}

¹Shanghai Branch, National Laboratory for Physical Sciences at Microscale and Department of Modern Physics, University of Science and Technology of China, Shanghai, 201315, China

²CAS Center for Excellence and Synergetic Innovation Center in Quantum Information and Quantum Physics, University of Science and Technology of China, Hefei, Anhui 230026, China

³CAS-Alibaba Quantum Computing Laboratory, Shanghai, 201315, China

⁴Department of Modern Physics, University of Science and Technology of China, Hefei, Anhui 230026, China



(Received 24 June 2020; accepted 18 August 2020; published 2 September 2020)

We apply a worm algorithm to simulate the quantum transverse-field Ising model in a path-integral representation of which the expansion basis is taken as the spin component along the external-field direction. In such a representation, a configuration can be regarded as a set of nonintersecting loops constructed by “kinks” for pairwise interactions and spin-down (or -up) imaginary-time segments. The wrapping probability for spin-down loops, a dimensionless quantity characterizing the loop topology on a torus, is observed to exhibit small finite-size corrections and yields a high-precision critical point in two dimensions (2D) as $h_c = 3.044\,330(6)$, significantly improving over the existing results and nearly excluding the central value of the previous result $h_c = 3.044\,38(2)$. At criticality, the fractal dimensions of the loops are estimated as $d_{\ell\downarrow}(1D) = 1.37(1) \approx \frac{11}{8}$ and $d_{\ell\downarrow}(2D) = 1.75(3)$, consistent with those for the classical 2D and 3D O(1) loop model, respectively. An interesting feature is that in one dimension (1D), both the spin-down and -up loops display the critical behavior in the whole disordered phase ($0 \leq h < h_c$), having a fractal dimension $d_\ell = 1.750(7)$ that is consistent with the hull dimension $d_H = \frac{7}{4}$ for critical 2D percolation clusters. The current worm algorithm can be applied to simulate other quantum systems like hard-core boson models with pairing interactions.

DOI: [10.1103/PhysRevB.102.094101](https://doi.org/10.1103/PhysRevB.102.094101)

I. INTRODUCTION

The quantum transverse-field Ising model (QTFI) is a textbook model in quantum many-body physics and plays an important role in quantum phase transition [1] and quantum information science [2]. The one-dimensional QTFI can be solved exactly [3], and it has been widely used to test theoretical or numerical methods [4,5] and to study novel quantities like entanglement entropy [6,7] and quantum fidelity susceptibility [8]. In higher dimensions, analytical results are scarce, and one has to rely on numerical or approximate methods. Many methods have been developed, including transfer-matrix method [9], series expansion [8,10], continuous-time Monte Carlo approach [5,11–15], tensor renormalization group method [16], density matrix renormalization group [17], projected entangled-pair states [18], and machine learning method [19,20], etc. Nevertheless, to obtain a high-precision critical point still remains to be a challenging task. To our knowledge, the best estimates of the critical point for the 2D QTFI are 3.044 2(4) in Ref. [8] and 3.044 38(2) in Ref. [5], achieved by *stochastic series expansion* (SSE) and continuous-time Wolff cluster methods, respectively.

In this work, we apply a worm algorithm to simulate QTFI in 1D and 2D. It is shown that as pointed out in Refs. [21,22],

the worm algorithm exhibits efficiency comparable to cluster schemes. A high-precision estimate of the square-lattice critical point is obtained as 3.044 330(6), significantly improving the existing results and nearly excluding the central value of 3.044 38(2) [5]. In the path-integral representation for the current worm algorithm, a configuration can be regarded as a set of nonintersecting loops constructed by “kinks” for pairwise interactions and spin-down (or -up) imaginary-time segments. Rich geometric properties are observed for these loops. In particular, it is found that in 1D, the loops over a wide parameter range exhibit scaling laws that are in the universality class of the classical 2D percolation. Deep theoretical understanding is desired. Further, a variety of physical quantities, including the magnetic and the fidelity susceptibilities, are examined.

The rest of the paper is organized as following. Section II explains the current path-integral representation for the QTFI and the formulation of the worm algorithm. The numerical results are presented in Sec. III. A brief summary is given in Sec. IV.

II. WORM ALGORITHM

The Hamiltonian of the QTFI on the d -dimensional cubic lattice is

$$\mathcal{H} = -t \sum_{\langle ij \rangle} \sigma_i^z \sigma_j^z - h \sum_i \sigma_i^x, \quad (1)$$

*jiangyi@ustc.edu.cn

†yjdeng@ustc.edu.cn

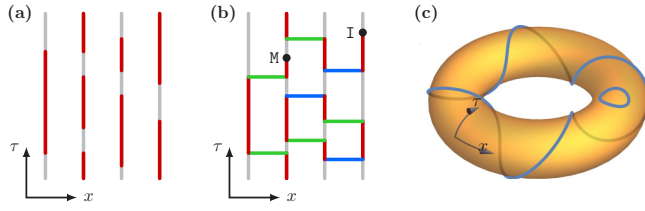


FIG. 1. Illustration of path-integral configurations. (a) For Eq. (1). Red (gray) segments represent the spin-up (-down) state. (b) A \mathcal{G} configuration for Eq. (8) in the rotated basis, having an open path with the two ends marked as I and M. Blue (green) lines are for pairing (hopping) kink. (c) A sketch of \mathcal{Z} configuration on the 1D torus, with a nonlocal loop of winding numbers ($\mathcal{W}_\tau = 4$, $\mathcal{W}_x = 1$). For simplicity, the lattice structure is not shown.

where σ_i^α ($\alpha = x, z$) are Pauli matrices, $\langle ij \rangle$ represents nearest-neighbor sites, $t > 0$ is the ferromagnetic interaction strength, and h is the transverse field. Taking the σ^z spin component as the expansion basis for the path-integral representation, one can map a d -dimensional QTFI onto a $(d+1)$ -dimensional classical system, for which each lattice site has a continuous line of spin segments; see Fig. 1(a) for an example. This continuous dimension is called the imaginary-time (τ) direction, along which the spin state σ_i^z can be flipped by the σ_i^x operator but must satisfy the periodic condition. The length of the τ dimension is the inverse temperature $\beta = 1/k_B T$ (the Boltzmann constant is set as $k_B = 1$ from now).

To formulate a worm algorithm that is effective for configurations of closed loops, we choose the external-field direction as the expansion basis and rewrite Hamiltonian (1) as

$$\mathcal{H} \equiv K + U = -t \sum_{\langle ij \rangle} \sigma_i^x \sigma_j^x - h \sum_i \sigma_i^z. \quad (2)$$

As a result, U and K are, respectively, the diagonal and the nondiagonal terms. The pairwise interactions $K = -t \sum_{\langle ij \rangle} \sigma_i^x \sigma_j^x$ can be further expressed in terms of the raising and lowering spin operators $\sigma^\pm = (\sigma^x \pm i\sigma^y)/2$, as

$$K \equiv K_1 + K_2 = -t \sum_{\langle ij \rangle} (\sigma_i^+ \sigma_j^- + \text{H.c.}) - t \sum_{\langle ij \rangle} (\sigma_i^+ \sigma_j^+ + \text{H.c.}). \quad (3)$$

The term K_1 flips a pair of opposite spins and thus the total magnetization is conserved along the τ direction, while K_2 flips a pair of spins of the same sign. We note that with the Holstein-Primakoff transformation, $b_i(b_i^\dagger) = \sigma_i^-(\sigma_i^+)$ and thus $n_i \equiv b_i^\dagger b_i = (\sigma_i^z + 1)/2$, the QTFI can be mapped onto a hard-core Bose-Hubbard (BH) model with Hamiltonian

$$\mathcal{H} = -t \sum_{\langle ij \rangle} (b_i^\dagger b_j + \text{H.c.}) - t' \sum_{\langle ij \rangle} (b_i^\dagger b_j^\dagger + \text{H.c.}) - \mu \sum_i n_i, \quad (4)$$

where $t' = t$, the particle number $n_i = 0, 1$, and the chemical potential $\mu = 2h$. In the language of the hard-core BH model, K_1 accounts for the hopping of a particle, and K_2 , which simultaneously creates/deletes a pair of particles, represents the pairing of two neighboring bosons. For convenience, we

shall refer to K_1 and K_2 as the hopping and the pairing term, respectively.

With Eq. (3), the partition function of Hamiltonian (2) can be formulated in the Feynman's path-integral representation (also called the world-line representation) as

$$\begin{aligned} \mathcal{Z} &= \text{Tr}[e^{-\beta\mathcal{H}}] = \sum_{\alpha_0} \langle \alpha_0 | e^{-\beta\mathcal{H}} | \alpha_0 \rangle \\ &= \lim_{\substack{d\tau = \beta/N \\ N \rightarrow \infty}} \sum_{\{\alpha_i\}} \langle \alpha_0 | e^{-\mathcal{H}d\tau} | \alpha_{N-1} \rangle \dots \langle \alpha_1 | e^{-\mathcal{H}d\tau} | \alpha_0 \rangle \\ &= \sum_{\alpha_0} \sum_{N=0}^{\infty} \int_0^\beta \int_{\tau_1}^\beta \dots \int_{\tau_{N-1}}^\beta \prod_{k=1}^N d\tau_k F(t, t', h) \end{aligned} \quad (5)$$

with the integrand function

$$F(t, t', h) = t^{\mathcal{N}_h} t'^{\mathcal{N}_p} \exp\left(-\int_0^\beta U(\tau) d\tau\right), \quad (6)$$

where \mathcal{N}_h and \mathcal{N}_p are, respectively, the number of hopping and pairing kinks ($\mathcal{N} = \mathcal{N}_h + \mathcal{N}_p$), $|\alpha_i\rangle = |\sigma_1^z, \sigma_2^z, \dots, \sigma_N^z\rangle$ is an eigenstate in the σ^z basis (N is the total number of lattice sites). Moreover, Eq. (5) can be graphically viewed as the summation/integration over configurations in the $(d+1)$ -dimensional space-time $\{i, \tau\}$, of which the statistical weight is

$$W_{\mathcal{Z}}(t, t', h) = \prod_{k=1}^N d\tau_k F(t, t', h). \quad (7)$$

In such a representation, each lattice site has a line of spin segments, and at imaginary time τ_k ($k = 1, 2, \dots, N$), a pair of neighboring spins is simultaneously flipped either by a hopping term K_1 or by a pairing term K_2 . We shall call them the hopping or the pairing kink, respectively. Starting from an arbitrary space-time point (i, τ) , one would construct a closed loop by following spin-up (-down) segments and kinks. Thus, a configuration effectively consists of closed loops.

An important ingredient of the worm algorithm is then to extend the configuration space \mathcal{Z} for Eq. (5) by including two defects. For the QTFI, the extended configuration space \mathcal{G} is for the spin-spin correlation function of the Pauli matrix σ^x :

$$\mathcal{G}(\mathbf{x}_I, \mathbf{x}_M, \tau_I, \tau_M) = \text{Tr}[T_\tau(\sigma_I^x(\tau_I) \sigma_M^x(\tau_M) e^{-\beta\mathcal{H}})], \quad (8)$$

where T_τ is the τ -ordering operator. In addition to closed loops, a path-integral configuration in the \mathcal{G} space contains an open path with two ending points; see an example in Fig. 1(b). We shall refer to the ending points as ‘‘Ira’’ (I) and ‘‘Masha’’ (M), and denote their coordinates in the space-time as (\mathbf{x}_I, τ_I) and (\mathbf{x}_M, τ_M) . The statistical weight of the \mathcal{G} configuration can be written as

$$W_{\mathcal{G}} = \frac{d\tau_I d\tau_M}{\omega_G} \prod_{k=1}^N d\tau_k F(t, t', h), \quad (9)$$

where F is given by Eq. (6) and ω_G is an arbitrary positive constant. When I coincides with M, the open path forms a closed loop, and the \mathcal{G} space is reduced to the \mathcal{Z} space.

The full configuration space for the worm-type simulation corresponds to the combination of the \mathcal{G} and the \mathcal{Z} spaces. For ergodicity, the simulation must be able to change the

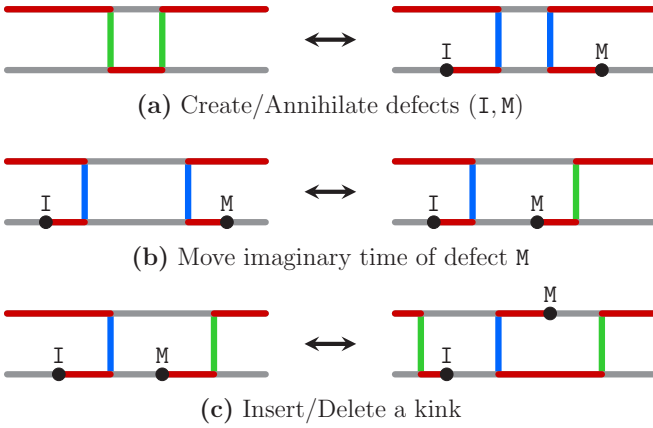


FIG. 2. The three updates.

kink number, the space-time location of any kink as well as of defects (I, M), and to switch configurations back and forward between the \mathcal{Z} and \mathcal{G} spaces. We adopt the following three updates: (a) create/annihilate defects (I, M), (b) move imaginary time of defect M, and (c) insert/delete a kink. The first operation switches configurations between the \mathcal{Z} and the \mathcal{G} spaces by creating or annihilating a pair of defects (I, M). The second updates the τ_M value, and the third changes the \mathbf{x}_M value by inserting or deleting a kink. Except “create defects (I, M),” all updates only apply in the \mathcal{G} space, and each of them is chosen with an *a priori* probability given before simulation.

(a) *Create/annihilate defects (I, M)*. If the current configuration is in the \mathcal{Z} space, “create defects (I, M)” is the only possible update. One randomly picks up a point (\mathbf{x}_I, τ_I) from the whole space-time volume $\beta N = \beta L^d$, draws a uniformly distributed imaginary-time displacement $\delta \in [-\tau_a/2, \tau_a/2)$ and $\delta \neq 0$ with the range $\tau_a \sim O(1/h)$ [23], assigns $\mathbf{x}_M = \mathbf{x}_I$ and $\tau_M = \text{mod}(\tau_I + \delta, \beta)$, and flips the spin state between defects I and M. The β periodicity is taken into account by the modular function. As illustrated in Fig. 2(a), the types (hopping or pairing) of kinks between defects I and M, if any, are interchanged during this operation.

The update “annihilate defects (I, M),” the reverse operation of “create defects (I, M),” is chosen with an *a priori* probability \mathcal{A}_a in the \mathcal{G} space. It changes a \mathcal{G} configuration into a \mathcal{Z} one by annihilating defects (I, M) and flipping the spin state in-between. This is possible only if I and M are on the same world line $\mathbf{x}_I = \mathbf{x}_M$ and their imaginary-time displacement $\min\{|\tau_I - \tau_M|, \beta - |\tau_I - \tau_M|\} \leq \tau_a/2$.

Accordingly, the detailed-balance condition reads as

$$\frac{d\tau_I}{\beta N} \frac{d\tau_M}{\tau_a} W_{\mathcal{Z}} \mathcal{P}_{\text{crea}} = \mathcal{A}_a W_{\mathcal{G}} \mathcal{P}_{\text{anni}}, \quad (10)$$

where $\mathcal{P}_{\text{crea}}$ ($\mathcal{P}_{\text{anni}}$) is the acceptance ratio for the “create defects” (“annihilate defects”) operation, $W_{\mathcal{Z}}$ ($W_{\mathcal{G}}$) is the statistical weight for the configuration before (after) the creation of defects, and $d\tau_I/(\beta N)$ and $d\tau_M/\tau_a$ account for the probability of choosing the space-time location for I and M, respectively.

Making use of Eqs. (7) and (9), the acceptance probabilities for the Metropolis filter can be calculated as

$$P_{\text{crea}} = \min \left[1, \mathcal{A}_a \tau_a \frac{\beta N F_{\text{new}}}{\omega_G F_{\text{old}}} \right], \quad (11)$$

$$P_{\text{anni}} = \min \left[1, \frac{1}{\mathcal{A}_a} \frac{1}{\tau_a} \frac{\omega_G F_{\text{new}}}{\beta N F_{\text{old}}} \right],$$

where F_{new} and F_{old} , given by Eq. (6), is respectively for the configuration after and before the corresponding operation. Note that the statistical-weight change $F_{\text{new}}/F_{\text{old}}$ is mainly determined by the random displacement $|\delta| \leq \tau_a/2$. As a result, the acceptance probabilities in Eq. (11) can be optimized by tuning τ_a .

A natural choice for the relative weight is $\omega_G = \beta N$ since the acceptance probabilities in Eq. (11) then hardly depend on L and β . Physically, this is because the spin-spin correlation function $\mathcal{G}(\mathbf{x}_I, \mathbf{x}_M, \tau_I, \tau_M)$ has the space-time translation invariance so that the statistical weight of a \mathcal{G} configuration should be normalized by the factor $1/\omega_G = 1/(\beta N)$. Further, with this choice, the number of Monte Carlo steps between two adjacent creations of (I, M), called the worm-return time, measures the ratio of the \mathcal{G} space over the \mathcal{Z} space, and exactly gives the dynamic magnetic susceptibility of the QTFI which is stated explicitly in Sec. III C.

(b) *Move imaginary time of defect M*. The update, reverse to itself, is chosen with a probability \mathcal{A}_b in the \mathcal{G} space. One randomly selects a time displacement $\delta \in [-\tau_b/2, \tau_b/2)$ and $\delta \neq 0$ assigns $\tau'_M = \text{mod}(\tau_M + \delta, \beta)$ for the new temporal location of defect M, and flips the spin states in-between; see Fig. 2(b). The types of in-between kinks are also interchanged. The acceptance probability is

$$P_{\text{move}} = \min \{1, F_{\text{new}}/F_{\text{old}}\}. \quad (12)$$

(c) *Insert/delete a kink*. Each operation is chosen with a probability \mathcal{A}_c in the \mathcal{G} space. In “insert a kink,” one randomly chooses one of the $z_d = 2d$ neighboring world lines of \mathbf{x}_M , say \mathbf{x}'_M , and updates the spatial location of M as $(\mathbf{x}_M, \tau_M) \rightarrow (\mathbf{x}'_M, \tau_M)$. Meanwhile, one inserts a kink k between world lines \mathbf{x}_M and \mathbf{x}'_M at imaginary time $\tau_k = \text{mod}(\tau_M + \delta, \beta)$, with a random displacement $\delta \in [-\tau_c/2, \tau_c/2)$ and $\delta \neq 0$. Further, the spin states between τ_M and τ_k , on both \mathbf{x}_M and \mathbf{x}'_M , are flipped which causes the types of in-between kinks, linking \mathbf{x}_M and \mathbf{x}'_M , to stay the same. However, the types of in-between kinks are interchanged if they link some other world lines to \mathbf{x}_M or \mathbf{x}'_M . An example is illustrated in Fig. 2(c).

In the reverse operation, “delete a kink,” one also picks up a random neighboring world line \mathbf{x}'_M of \mathbf{x}_M and moves M as $(\mathbf{x}_M, \tau_M) \rightarrow (\mathbf{x}'_M, \tau_M)$. Further, one counts the number n_k of kinks that connect world lines \mathbf{x}_M and \mathbf{x}'_M in the imaginary-time domain $[\tau_M - \tau_c/2, \tau_M + \tau_c/2)$. If no kink exists $n_k = 0$, the operation is rejected. Otherwise, one randomly picks up one of the n_k kinks and deletes it, and meanwhile flips the spin states on both world lines between τ_M and the imaginary time of the deleted kink. Besides types of kinks linking \mathbf{x}_M or \mathbf{x}'_M to other world lines are interchanged as well.

The detailed balance condition of this pair of operations reads as

$$\mathcal{A}_c \frac{1}{z_d} \frac{d\tau_k}{\tau_c} W \mathcal{P}_{\text{inse}} = \mathcal{A}_c \frac{1}{z_d} \frac{1}{n_k} W_+ \mathcal{P}_{\text{dele}}, \quad (13)$$

where $\mathcal{P}_{\text{inse}}$ ($\mathcal{P}_{\text{dele}}$) is for the acceptance ratio for “insert a kink” (“delete a kink”). The statistical weights W and W_+ , given by Eq. (9), are respectively for the configuration before and after inserting a kink. The infinitesimal $d\tau_k$ on the left-hand side is canceled by W_+ , which has one more kink. The acceptance probabilities are then

$$\begin{aligned} P_{\text{inse}} &= \min \left[1, \frac{\tau_c}{n_k + 1} \frac{F_{\text{new}}}{F_{\text{old}}} \right], \\ P_{\text{dele}} &= \min \left[1, \frac{n_k}{\tau_c} \frac{F_{\text{new}}}{F_{\text{old}}} \right], \end{aligned} \quad (14)$$

where n_k denotes the number of in-between kinks for the current configuration. The denominator $n_k + 1$ in P_{inse} reflects an extra kink in the updated configuration.

The worm algorithm is then formulated as in Algorithm 1, in which *a priori* probabilities satisfy $\mathcal{A}_a + \mathcal{A}_b + 2\mathcal{A}_c = 1$. It is mentioned again that the acceptance probabilities in the updates can be optimized by tuning the ranges of random τ displacement, τ_a , τ_b , and τ_c . As its analog for the classical Ising model which carries out a weighted random walk over the lattice, the defect M in this quantum Monte Carlo method effectively performs a random walk in the space-time and simultaneously updates the spin states it passes by.

For the conventional BH model which does not have the pairing term, the interchange between the hopping and pairing kink cannot be allowed. For “create/annihilate defects” and “move imaginary time of M ,” the above illegal updates can be avoided when performing these operations *only* within a larger spin segment. In “insert/delete a kink,” the simplest remedy is that the proposed update is rejected as long as it leads to an illegal configuration, giving a price that the acceptance probabilities are decreased by a factor of $O(1/h)$. As a more sophisticated remedy, one can reformulate the operation in a way such that no illegal configuration would be introduced.

Finally, for the computational efficiency, it is important to implement hash tables such that each operation is done within $O(1)$ CPU time.

III. NUMERICAL RESULTS

In the absence of the external field ($h = 0$), the spin-up and -down states are fully balanced in the QTFI (2). As h turns on, the system evolves into a disordered phase with the spin-down state being suppressed and the spin-up order still not formed ($h < h_c$). It enters into the spin-up ordered phase ($h > h_c$) through a second-order quantum phase transition. The critical point is exactly known as $h_c/t = 1$ in 1D and numerically determined as $h_c/t \approx 3.044$ in 2D (square lattice). Without loss of generality, the pairwise interaction is set as $t = 1$ from now unless stated explicitly.

Using the worm algorithm, we simulate the 1D and 2D QTFIs with linear lattice size L and inverse temperature $\beta = L$; the choice of $\beta = L$ is due to the dynamic critical exponent $z = 1$ for the QTFI. Periodic boundary conditions are applied in each spatial direction, so that the lattice is essentially a torus. The linear size is taken up to $L = 512$ in 1D and $L = 128$ in 2D, and no severe critical slowing down is observed. A variety of geometric and physical quantities are sampled. To

locate the phase transition h_c , we make use of the topological properties of the nonintersecting loops on the torus, instead of the scaling behaviors of physical quantities like the magnetic susceptibility.

A. Critical point

Given a \mathcal{Z} configuration, we record how many times $\mathcal{W}_i^\ell \geq 0$ each loop ℓ winds along the i th direction ($i = 1, 2, \dots, d$), and calculate the total winding number $\mathcal{W}_i = \sum_\ell \mathcal{W}_i^\ell$ from all the loops; see Fig. 1(c) for an illustration. A path-integral configuration is said to wrap along the i th direction as long as $\mathcal{W}_i > 0$. This is indicated as $\mathcal{R}_i = 1$; otherwise, $\mathcal{R}_i = 0$. The average wrapping probability $R = (1/d) \sum_i \langle \mathcal{R}_i \rangle$ is then calculated, with $\langle \cdot \rangle$ representing the ensemble average. In the sub-percolating phase, the loops are too small to percolate, and the R value quickly drops to 0 as L becomes larger. In the superpercolating phase, there is at least one giant loop with large \mathcal{W}_i^ℓ , and the R value rapidly converges to 1. At the percolation threshold, the R values for different system sizes L have an asymptotically common intersection with a nontrivial value between 0 and 1. In short, the wrapping probability R is a dimensionless quantity characterizing the topological feature of loops on torus. In many cases, such wrapping probabilities are found to exhibit small finite-size corrections, and have been widely used for locating critical points [24–28].

Algorithm 1 Worm algorithm

BEGIN: Given a \mathcal{Z} configuration.

loop

if it is a \mathcal{Z} configuration

 choose the “create defects (I, M)” operation

else

 choose an operation with its *a priori* probability except “create defects (I, M)”

end if

 calculate the acceptance probability P and carry out the operation with the probability P

end loop

For the QTFI, two types of nonintersecting loops, spin-up (\uparrow) or -down (\downarrow) loops, can be constructed. The Monte Carlo (MC) results in Fig. 3 show that irrespective of the spatial dimension (1D or 2D), both the spin-up and -down loops display critical behaviors near the quantum critical point h_c . In 1D, particularly rich behaviors are observed. In the whole disordered phase ($0 \leq h < h_c$), both R_\uparrow and R_\downarrow have nontrivial values, $0 < R_\uparrow(R_\downarrow) < 1$, indicating the fractal structures of these loops. At the transition point $h = h_c$, the R_\uparrow and R_\downarrow values have a sharp drop, which becomes infinitely sharp for $L \rightarrow \infty$. For $h > h_c$, the R_\downarrow value drops to 0, meaning that the spin-down loops are too small to percolate, while the R_\uparrow value converges to nontrivial value if h is not too large, suggesting that the spin-up loops still exhibit fractal properties. Nevertheless, as h is further increased, the R_\uparrow value also gradually approaches to 0. This is understandable because the number of kinks decreases when h increases, and thus the spin loops are less likely to percolate. In 2D, the R_\uparrow and

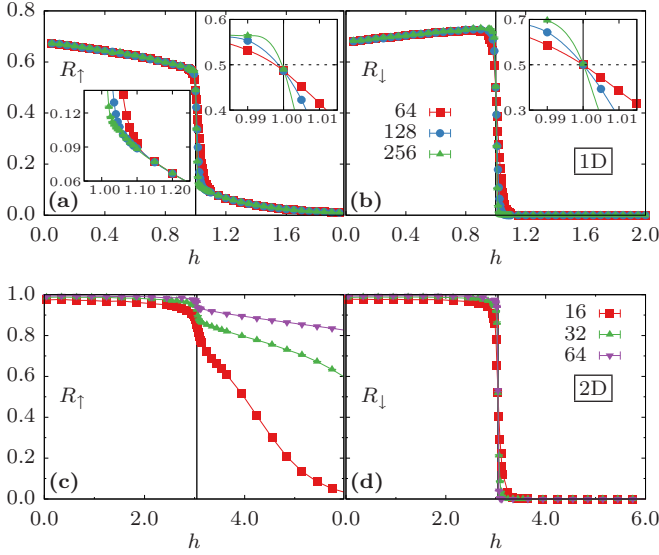


FIG. 3. Wrapping probabilities R_\uparrow and R_\downarrow versus the transverse field h . The error bars are much smaller than the size of points. The vertical black lines indicate the critical point. (a), (b) are for 1D, and (c), (d) are for 2D. The inset plots of (a) and (b) show the curve near $h_c = 1$.

R_\downarrow values converge to 1 in the disordered phase $0 \leq h < h_c$, suggesting a superpercolating phase both for the spin-up and -down loops. For $h > h_c$, the R_\downarrow value quickly reaches 0, but R_\uparrow seems to converge to 1 for $L \rightarrow \infty$. At $h = h_c$, the R_\downarrow value has a sharp drop, and the derivative of R_\uparrow with respect to h probably also develops a singularity as L increases.

Extensive simulations are then carried out at $h = h_c = 1$ in 1D and $h = 3.04435$ in 2D, and the data nearby are obtained by the standard reweighting technique [29]. The system size is taken as $L = 16, 64, 256, 512$ in 1D, with at least 4×10^8 samples for each L , and $L = 8, 16, 32, 64, 128$ in 2D, with at least 1×10^8 samples for each L .

According to the least-squares criterion, the R_\downarrow data, partly shown in Figs. 4 and 5, are fitted by

$$R_\downarrow = R_{\downarrow,c} + \sum_{k=1}^2 a_k (h - h_c)^k L^{ky_i} + b_i L^{y_i} + b_2 L^{y_2}. \quad (15)$$

The thermal renormalization exponents are fixed at the known values in the classical $(d + 1)$ Ising universality, i.e., $y_i(1D) = 1$ and $y_i(2D) = 1.5868$ [30]. The term with b_i comes from the leading irrelevant thermal field, which has the exponent $y_i(1D) = -2$ and $y_i(2D) = -0.821$ [28,30]. The subleading correction exponents are set as $y_2(1D) = -3$ and $y_2(2D) = -2$. As a precaution, we gradually increase L_{\min} and exclude the $L < L_{\min}$ data from the fit to see how the ratio of the residual χ^2 to the degree of freedom changes with L_{\min} .

In 1D, it is found that the MC data for $L_{\min} = 64$ can be well described by Eq. (15) without the correction-to-scaling term ($b_2 = 0$). The fit yields $h_c = 1.000\,001(5)$, in excellent agreement with the exact quantum critical point $h_c = 1$. Also, we have $R_{\downarrow,c} = 0.4995(3)$, which suggests that it might exactly be $\frac{1}{2}$; see the inset of Fig. 3(b).

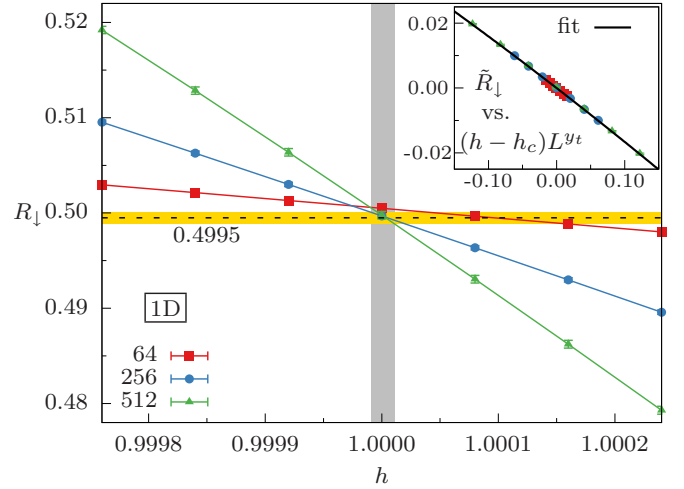


FIG. 4. Wrapping probability R_\downarrow in 1D. The gray band indicates an interval of 2σ above and below the estimate $h_c = 1.000\,001(5)$. The yellow band indicates an interval of 2σ above and below the estimate $R_c = 0.4995(3)$. The inset shows $\tilde{R}_\downarrow = R_\downarrow - R_c - b_i L^{y_i}$ versus $(h - h_c)L^{y_i}$, with $a_1 = -0.1625(9)$, $a_2 = -0.34(13)$, $b_i = 4.3(1.5)$, $y_i = -2$, and $y_i = 1$.

In 2D, an eye-view fitting of the R_\downarrow data in Fig. 5 already gives the critical point approximately as $h_c \approx 3.044\,33$, with uncertainty at the fifth decimal place. We find that it is sufficient to describe these data by Eq. (15) with $a_2 = 0$ which means the fit is linear and for $L_{\min} = 16$, b_2 can also be set to zero. The fit gives $R_{\downarrow,c} = 0.528\,1(14)$ and $h_c = 3.044\,330(6)$. To test the reliability of the value and the error bar of h_c , we plot in Fig. 6 the R_\downarrow data against L at some fixed h near h_c . It can be seen that at $h = h_c = 3.044\,330$, the wrapping probability R_\downarrow converges to a constant value within the 2σ shadow area in Fig. 6. In contrast, as L increases, the R_\downarrow data

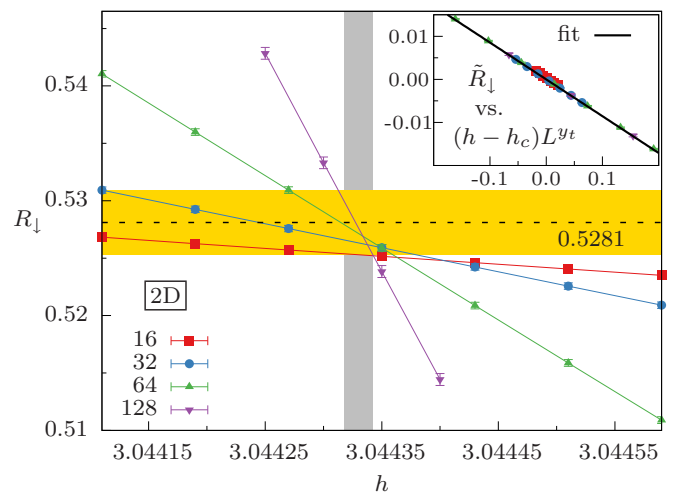


FIG. 5. Wrapping probability R_\downarrow in 2D. The gray band indicates an interval of 2σ above and below the estimate $h_c = 3.044\,330(6)$. The yellow band indicates an interval of 2σ above and below the estimation $R_c = 0.528\,1(14)$. The inset displays $\tilde{R}_\downarrow = R_\downarrow - R_c - b_i L^{y_i}$ versus $(h - h_c)L^{y_i}$, with $a_1 = -0.0855(8)$, $b_i = -0.031(8)$, $y_i = -0.821$, and $y_i = 1.568$.

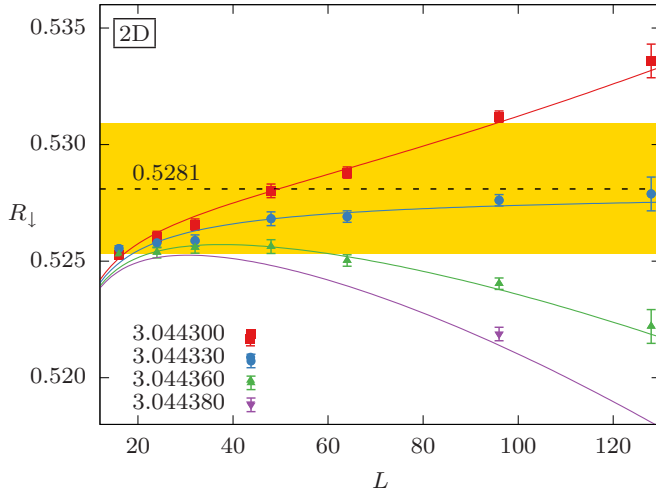


FIG. 6. Plot of R_{\perp} versus L for various values of h for the 2D QTFI. The yellow strip indicates an interval of 2σ above and below the estimate $R_{\perp,c} = 0.5281(14)$. The solid lines are plotted according to the fitting result.

for $h = 3.044300$ and 3.044360 bend upward and downward, respectively, suggesting that they are clearly away from the thermodynamic critical point. For $h = 3.04438$, which is the estimated central value of the critical point in Ref. [5], the downward bending is stronger, meaning that it cannot be the critical point. Table I gives a (incomplete) list of the existing results for h_c in 2D. It is clear that our estimate has the highest precision.

We now briefly discuss the efficiency of the current worm algorithm, which is already reflected by the precision of the estimated critical point h_c . For a quantitative evaluation, we calculate at criticality the integrated autocorrelation times τ_{int} for the energy \mathcal{E} , magnetization \mathcal{M} , and kink number \mathcal{N}_k , in the unit of MC sweeps. A MC sweep is defined such that on average, each imaginary-time spin line is updated by βt times. From the least-squares fitting $\tau \propto L^{z_o}$, we obtain the dynamical exponent as $z_{\mathcal{E}} = 0.38(3)$, $z_{\mathcal{M}} = 0.35(3)$, and $z_{\mathcal{N}_k} = 0.41(3)$ for 1D, and $z_{\mathcal{E}} = 0.28(3)$, $z_{\mathcal{M}} = 0.23(4)$, and

TABLE I. Estimated critical point h_c on the square lattice. CMC: cluster Monte Carlo method; SSE: stochastic series expansion; S-W: Swendsen-Wang in continuous time; HOSVD: tensor renormalization group method based on the higher-order singular value decomposition; iPEPS: infinity projected entangled-pair state; MERA: multiscale entanglement renormalization ansatz; CTM: corner transfer matrix.

Method	h_c
This work	3.044 330(6)
CMC [5]	3.044 38(2)
SSE [8]	3.044 2(4)
S-W [11]	3.044(1)
HOSVD(D=14) [16]	3.043 9
iPEPS [31]	3.04
MERA [32]	3.075
CTM [33]	3.14

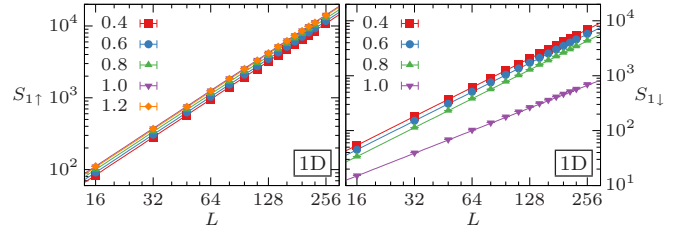


FIG. 7. The largest-loop size $S_{1\uparrow}$ and $S_{1\downarrow}$ versus L at $h = 0.4, 0.6, 0.8, 1.0, 1.2$ for 1D. For $S_{1\uparrow}$, the straight lines have a slope $\frac{7}{4}$, irrespective of the h value. For $S_{1\downarrow}$, the lines have slope $\frac{7}{4}$ for $h < h_c$ and $\frac{11}{8}$ for $h = h_c$.

$z_{\mathcal{N}_k} = 0.30(3)$ for 2D. The efficiency of the worm algorithm is comparable to that of the Wolff-type cluster method [5]. Note that as the spatial dimension increases, all the values of z_o decrease. From the numerical results of the worm algorithm for the classical Ising model [21,34], we expect $z_o = 0$ (without critical slowing down) for $d \geq d_c$, where $d_c = 3$ is the upper critical dimensionality for the QTFI.

B. Geometric properties of loops

We have determined the quantum critical point h_c with a high precision by locating the percolation threshold of the loop configurations. Hereby, we shall further explore other geometric properties of the spin-up and -down loops at and away from h_c . In the \mathcal{Z} space, we measure the average length S_1 of the largest loop and the probability distribution that a randomly chosen loop is of size s , i.e., $P(s, L) \equiv (1/N_{\ell}(L))\partial N_{\ell}(s, L)/\partial s$, where $N_{\ell}(L) \sim \beta L^d$ is the total number of loops and $N_{\ell}(s, L)$ is the number of loops of size in range $(s, s + ds)$.

In 1D, one knows from Fig. 3 that for the whole region $0 \leq h \leq h_c$, both the spin-up and -down loops exhibit critical scaling behaviors. For the spin-up loops, such fractal properties further survive in the ordered phase $h > h_c$. In these cases, we expect that the largest-loop size scales as $S_1 \propto L^{d_{\ell}}$, where $d_{\ell} < (1 + 1)$ is the loop fractal dimension, and that the loop-size distribution behaves as [35,36]

$$P(s, L) \sim s^{-\tau} f(s/L^{d_{\ell}}), \quad (16)$$

where τ is called the Fisher exponent. Moreover, the exponents τ and d_{ℓ} are related by the hyperscaling relation $\tau = 1 + (d + 1)/d_{\ell}$. The function $f(x \equiv s/L^{d_{\ell}})$ is universal and describes the finite-size cutoff of s near $S_1 \sim L^{d_{\ell}}$.

We simulate at $h = 0.4, 0.6, 0.8, 1.0, 1.2$ and the results are shown in Fig. 7. The straight lines in the log-log plot suggest that indeed, the largest loop has a fractal structure. For the spin-up loops, irrespective of the h value, the straight lines have the same slope approximately as $\frac{7}{4}$. Further, the amplitude of the power law $S_{1\uparrow} \sim L^{7/4}$ increases as a function of h , at least in the range of $0.4 \leq h \leq 1.2$. In contrast, as h increases, the largest-loop size $S_{1\downarrow}$ decreases and then drops to a significantly smaller value at $h = h_c$. Further, while the lines for $h < h_c$ still have a slope near $\frac{7}{4}$, the line for $h = h_c$ has a smaller slope which is about $\frac{11}{8}$. This suggests that the spin-down loops start with a dense and critical phase for $h < h_c$, experience a critical state at $h = h_c$, and then enter

TABLE II. Estimates of $d_{\ell\uparrow}$ and $d_{\ell\downarrow}$ at different h in 1D.

h	0.4	0.6	0.8	$1.0(h_c)$	1.2
$d_{\ell\uparrow}$	1.754(6)	1.750(5)	1.747(5)	1.750(6)	1.751(3)
$d_{\ell\downarrow}$	1.751(5)	1.749(7)	1.750(7)	1.37(1)	

into a sparse phase containing enormous small loops. The S_1 data for both the spin-up and -down loops are fitted by

$$S_1 = L^{d_\ell} (a_0 + b_1 L^{y_1}), \quad (17)$$

with different choices of the correction exponent $y_1 = -0.5, -1.0, \text{ or } -1.5$. We find that the fits are rather stable, and the results are shown in Table II.

We notice that the configuration of the classical $O(n)$ loop model on the honeycomb lattice also consists of non-intersecting loops [37–39]. Moreover, the $O(n)$ loop model with $n = 1$ corresponds to the 2D Ising model, and has a hull/loop dimension as $d_{\text{hull}} = \frac{11}{8}$ at the critical point $x_c = 1/\sqrt{2 + \sqrt{2 - n}} = 1/\sqrt{3}$ and $d_{\text{hull}} = \frac{7}{4}$ in the dense phase $x > x_c$, where x is the statistical weight for each loop unit [37–39]. These behaviors are very similar to those of the spin-down loops for the 1D QTFI. Accordingly, we conjecture that in 1D, the fractal dimensions $d_{\ell\downarrow}(h = h_c) = 1.37(1)$ and $d_{\ell\downarrow}(h < h_c) = 1.750(6)$ are exactly identical to $\frac{11}{8}$ and $\frac{7}{4}$, respectively. We also conjecture that the fractal dimension $d_{\ell\uparrow} = 1.747(5)$, which is independent of the h value, is also exactly equivalent to $\frac{7}{4}$. Further, it is noted that by the duality relation, the loops on the honeycomb lattice can be mapped onto the boundaries of the spin domains for the Ising model on the triangular lattice. In the dense phase $x > x_c$, these domains are simply *critical* site-percolation clusters. Therefore, we expect that the domains, enclosed by the spin-up or -down loops, are also fractal and have a fractal dimension corresponding to that for critical Ising spin domains or percolated clusters in 2D.

To further demonstrate the fractal structure of the spin-up and -down loops in 1D, we display in Fig. 8 the MC data for the loop-size distribution $P(s, L)$. Indeed, one observes algebraically decaying behaviors $s^{-\tau}$ for the spin-up loops with $h = 0.8, 1.0, 1.2$ and for the spin-down loops with $h = 0.8, 1.0$. The cutoff size of s for the power-law scaling, due to finite-size effects, increases as the system size L . The hyperscaling relation $\tau = 1 + (d + 1)/d_\ell$ is well confirmed by the fact that the data for different L collapse onto the straight lines with slope $-\frac{15}{7}$ or $-\frac{27}{11}$. For the spin-down loops in the ordered phase $h = 1.2$, the $P(s, L)$ data for different L drop quickly, illustrating that the loop sizes are finite even in the thermodynamic limit $L \rightarrow \infty$. We further plot $s^\tau P(s, L)$ versus s/L^{d_ℓ} in Fig. 9. With the values of (d_ℓ, τ) as $(\frac{7}{4}, \frac{15}{7})$ or $(\frac{11}{8}, \frac{27}{11})$, the data for different L collapse well onto a single curve, illustrating the universal feature of the cutoff function $f(x)$. It is interesting to see that for the spin-down loops at $h = h_c$, function $f(x)$ displays a two-peak structure [Fig. 9(b')]. We regard that the first peak at the smaller value of x reflects the residual effect of the spin-down loops in the disordered phase $h < h_c$. Meanwhile, it is observed that for the spin-up loops with $h = 1.2$, function $f(x)$ exhibits a shoulder feature

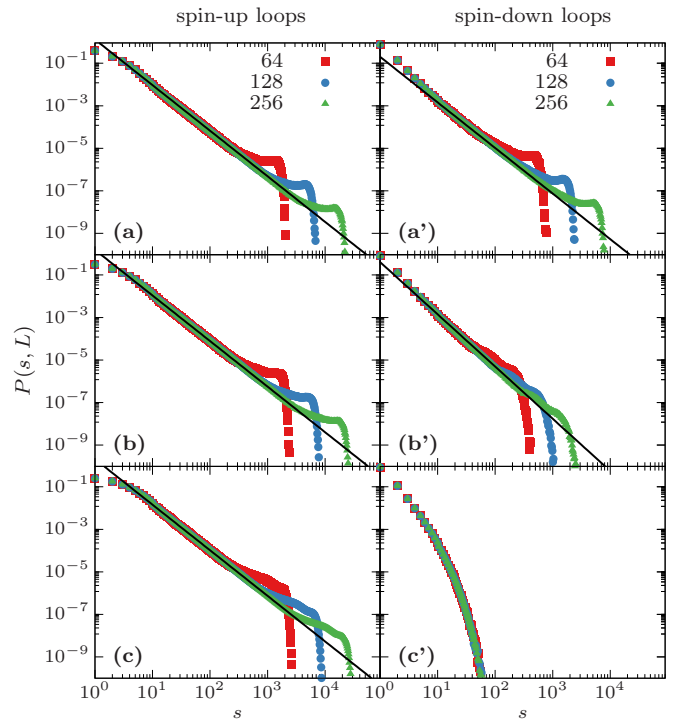


FIG. 8. Loop-size distribution $P(s, L)$ for different h values in 1D. The figures in the left (right) panel are for the spin-up (-down) loops, and the first, second, and third rows correspond to $h = 0.8, 1.0, 1.2$, respectively. The straight lines, with slope $-\frac{15}{7}$ or $-\frac{27}{11}$, are a guide for the eye.

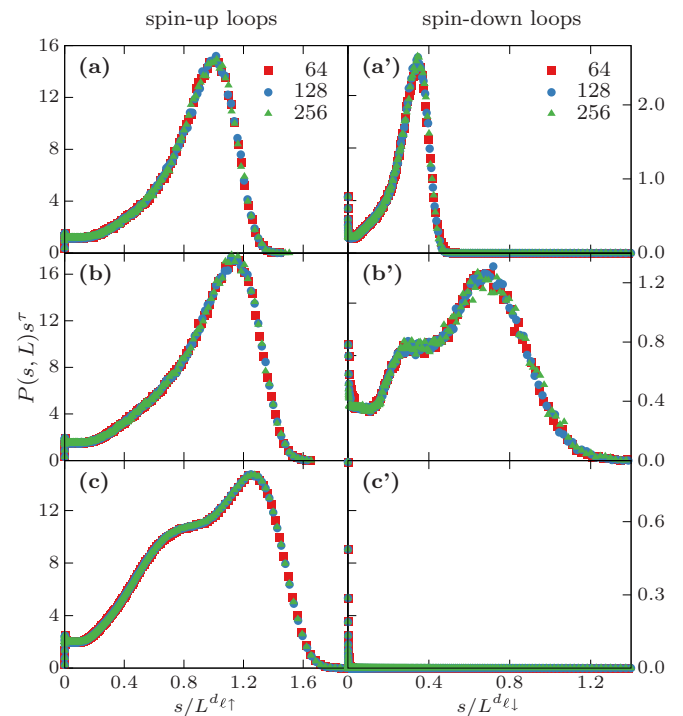


FIG. 9. $P(s, L)s^\tau$ versus s/L^{d_ℓ} in 1D. The plots in the left (right) panel are for the spin-up (-down) loops, and the first, second, and third rows correspond to $h = 0.8, 1.0, 1.2$, respectively. The values of $d_{\ell\uparrow}$ and $d_{\ell\downarrow}$ are listed in Table II, and the τ value is calculated from the hyperscaling relation $\tau = 1 + (d + 1)/d_\ell$.

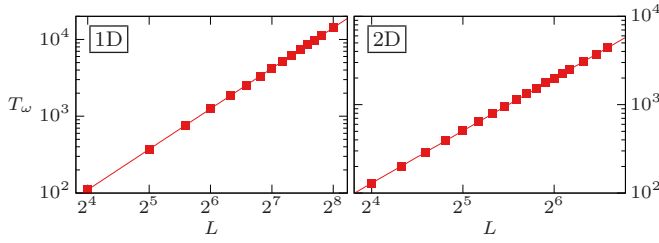


FIG. 10. Worm-return time at criticality h_c . The straight lines, with slope $2y_h - (d + 1)$, are a guide for the eye.

on the smaller- x side. We expect that as h increases, such a shoulder feature would become more pronounced and its location would move toward the value $x = 0$. This is because that as h is enhanced, the number of kinks will be gradually suppressed and the sizes of the spin-up loops will eventually start to decrease. In the limiting case $h \rightarrow \infty$, all the spin-up loops will become individual imaginary-time lines with length β .

In 2D, the spin-down loops are fractal only at $h = h_c$, and the spin-up loops are always in a superpercolating phase. The fit of the $S_{1\downarrow}$ data by Eq. (17) gives $d_{\ell\downarrow} = 1.75(3)$. Again, this is in excellent agreement with the loop dimension $d_{\text{hull}} = 1.734(4)$ for the classical $O(n = 1)$ loop model on the 3D *hydrogen-peroxide* lattice [40], on which the loops are also nonintersecting. As expected, for the spin-down loops at $h = h_c = 3.044\,330$, the loop-size distribution $P(s, L)$ follows Eq. (16).

C. Worm-return time

The worm-return time T_w is the average update steps between two adjacent \mathcal{Z} configurations in the markov chain MC simulation. Mathematically, it can be expressed as the integral of spin-spin correlation function (8) over the lattice and the imaginary time as

$$\begin{aligned} T_w &= \frac{1}{\omega_G \mathcal{Z}} \text{Tr} \left[T_\tau \int_0^\beta \int_0^\beta d\tau_i d\tau_m \sum_{\mathbf{x}_i, \mathbf{x}_m} \sigma_i^x(\tau_i) \sigma_m^x(\tau_m) e^{-\beta \mathcal{H}} \right] \\ &= \frac{1}{\omega_G \mathcal{Z}} \text{Tr} \left[\left(\int_0^\beta d\tau \sum_i \sigma_i^x(\tau) \right)^2 e^{-\beta \mathcal{H}} \right] \\ &= \frac{1}{\omega_G \mathcal{Z}} \text{Tr} \left[\left(\int_0^\beta d\tau M^x(\tau) \right)^2 e^{-\beta \mathcal{H}} \right]. \end{aligned} \quad (18)$$

With the choice of $\omega_G = \beta N$, the worm-return time T_w is precisely equal to the dynamic magnetic susceptibility $\chi^{xx} = \langle [\int_0^\beta d\tau M^x(\tau)]^2 \rangle / \beta N$. Figure 10 shows the T_w data at $h = h_c$ for both 1D and 2D, which are fitted by

$$T_w = L^{2y_h - (d+1)} (a_0 + b_1 L^{y_i}). \quad (19)$$

In 1D, the fit with $y_i = -2$ gives $y_h = 1.876(2)$, in excellent agreement with the exact value $\frac{15}{8}$. In 2D, we set $y_i = -0.821$ [30] and obtain $y_h = 2.484(4)$, which is again well consistent with the result $y_h = 2.4816(1)$ for the classical 3D Ising model [30].

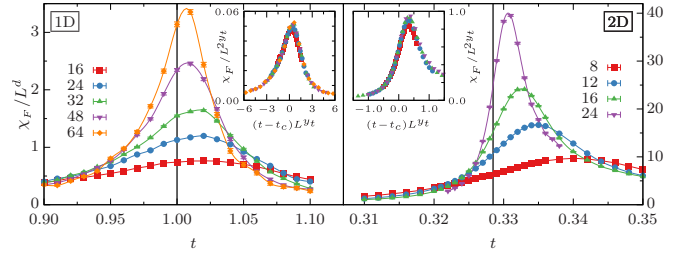


FIG. 11. Fidelity susceptibility $\chi_F(t)$ versus t , with (a) for 1D and (b) for 2D. The black solid lines indicate the critical points $t_c(1D) = 1$ and $t_c(2D) = 1/3.044\,330$. The insets show χ_F/L^{2y_i} versus $(t - t_c)L^{y_i}$ which indicate the universality of the function $f_{\chi_F}(x)$.

D. Fidelity susceptibility

It is well known that many systems can undergo quantum phase transitions without spontaneous symmetry breaking and thus without a good definition of local order parameter. These phase transitions are beyond the Ginzburg-Landau paradigm, and are difficult to be detected by conventional thermodynamic observables. Fidelity susceptibility, a quantity proposed in the quantum information science [41], has been shown to be useful for such a purpose [8,42–45]. Consider a quantum phase transition driven by some given parameter λ and let $|\phi(\lambda)\rangle$ represent the corresponding wave function, the fidelity $F(\lambda, \epsilon)$ of the system is defined as the overlap between the wave functions with different values of λ , i.e., $F(\lambda, \epsilon) = |\langle \phi(\lambda) | \phi(\lambda + \epsilon) \rangle|$. Accordingly, the fidelity susceptibility $\chi_F(\lambda)$ is calculated as

$$\chi_F(\lambda) = - \left. \frac{\partial^2 \ln F(\lambda, \epsilon)}{\partial \epsilon^2} \right|_{\epsilon=0}. \quad (20)$$

For the QTFI, we hereby choose the driving parameter λ to be the pairwise interaction t , which is conjugate to the number of kinks \mathcal{N}_k . Given a \mathcal{Z} configuration, let $\mathcal{N}_{k,1}$ and $\mathcal{N}_{k,2}$ denote the total number of kinks in the first-half imaginary-time domain $0 \leq \tau < \beta/2$ and the second-half one $\beta/2 \leq \tau < \beta$, respectively. It can be shown by following Ref. [43] that the fidelity susceptibility $\chi_F(t)$ is proportional to the covariance of $\mathcal{N}_{k,1}$ and $\mathcal{N}_{k,2}$, and can be written as

$$\chi_F(t) = \frac{\langle \mathcal{N}_{k,1} \mathcal{N}_{k,2} \rangle - \langle \mathcal{N}_{k,1} \rangle \langle \mathcal{N}_{k,2} \rangle}{2t^2}, \quad (21)$$

where the external field h is now set to be 1. The MC data of $\chi_F(t)$ for the 1D and 2D QTFI are shown in Fig. 11. As expected, the $\chi_F(t)$ data for each L display a peak near the critical point t_c . As system size L increases, the peak location t_L , called the pseudocritical point, moves toward the thermodynamic critical point t_c , and the peak itself becomes sharper with a smaller width. Following the standard finite-size scaling analysis, we expect that near the critical point t_c , the fidelity susceptibility χ_F scales as

$$\chi_F(t, L) = L^{2y_i} f_{\chi_F}(L^{y_i}(t - t_c)). \quad (22)$$

Indeed, making use of $y_i(1D) = 1$ and $y_i(2D) = 1.5868$, we obtain a good collapse when plotting χ_F/L^{2y_i} versus $(t - t_c)L^{y_i}$, as shown in the insets of Fig. 11.

For the fidelity $F(\lambda, \epsilon)$, we can also choose the driving parameter to be the external field h for the QTFI, which is

conjugate to the σ^z -component magnetization \mathcal{M} . In this case, we should consider the magnetization \mathcal{M}_1 for $0 \leq \tau < \beta/2$ and \mathcal{M}_2 for $\beta/2 \leq \tau < \beta$, and the fidelity susceptibility $\chi_F(h)$ would be proportional to the covariance of \mathcal{M}_1 and \mathcal{M}_2 . At the critical point, we expect $\chi_F \propto L^{2y_h}$.

While Fig. 11 illustrates the applicability of the fidelity susceptibility χ_F as a tool for studying the quantum phase transition, it is worth mentioning that by calculating the covariance of two quantities of the same kind but in separated spatial/imaginary-time domains, χ_F normally has large fluctuations. Thus, to achieve a good statistics for χ_F would require extensive simulations.

IV. DISCUSSION

We formulate a worm-type algorithm and study the QTFI in a path-integral representation in which configurations are sets of nonintersecting loops. By locating the percolation threshold of loop configurations via the so-called wrapping probability, we obtain a high-precision quantum critical point $h_c = 3.044\,330(6)$ for the QTFI on the square lattice. These nonintersecting loops are further observed to exhibit rich geometric properties, particularly in 1D, where both the spin-up and -down loops have fractal structures over a wide parameter range. By examining the similarity of the scaling behaviors for the d -dimensional QTFI and for the $(d+1)$ -dimensional classical $O(n=1)$ model, we conjecture that in 1D the two fractal dimensions are $d_{\ell\downarrow}(h_c) = \frac{11}{8}$ and $d_{\ell\downarrow}(h < h_c) = \frac{7}{4}$, and that in 2D, $d_{\ell\downarrow}(h_c) = 1.75(3)$ is equal to the hull dimension $d_{\text{hull}} = 1.734(4)$ for the classical 3D loop model. The finite-size scalings of magnetic and fidelity susceptibilities are also examined. It is confirmed that the fidelity susceptibility can be used to probe quantum phase transitions.

Motivated by the fact that the classical $O(1)$ loop model is a specific case of the $O(n)$ loop model with $n=1$, we can generalize the loop path-integral representation of the QTFI by giving each spin-down loop a statistical weight n . As a consequence, the partition function (5) is generalized to be

$$\mathcal{Z}(t, t', h, n) = \sum_{\{\alpha_0\}} \sum_{N=0}^{\infty} \int_0^{\beta} \int_{\tau_1}^{\beta} \dots \int_{\tau_{N-1}}^{\beta} \prod_{k=1}^N d\tau_k \times n^{N_{\ell\downarrow}} t^{N_h} t'^{N_p} e^{-\int_0^{\beta} U(\tau) d\tau}$$

$$= C \sum_{\{\alpha_0\}} \sum_{N=0}^{\infty} \int_0^{\beta} \int_{\tau_1}^{\beta} \dots \int_{\tau_{N-1}}^{\beta} \prod_{k=1}^N d\tau_k \times n^{N_{\ell\downarrow}} t^{N_h} t'^{N_p} (e^{-2h})^{\mathcal{S}_{\ell\downarrow}}, \quad (23)$$

where $C = e^{h\beta N}$, $N_{\ell\downarrow}$ specifies the number of spin-down loops, and $\mathcal{S}_{\ell\downarrow}$ is the total length of spin-down loops. We expect that for $t = t'$, the phase transition of such a ‘‘quantum $O(n)$ loop’’ model in d dimensions will belong to the same universality class as that for the classical $O(n)$ loop model in $(d+1)$ dimensions. In 1D, we further expect that the exact value of the quantum critical point $h_c(n)$ can be obtained for the ‘‘quantum $O(n)$ loop’’ model, and that the spin-down loops would exhibit rich geometric properties both at criticality $h_c(n)$ and in the disordered phase $h < h_c$. In particular, for $(d=1, n=2)$, the phase transition would be of the celebrated Berezinskii-Kosterlitz-Thouless topological transition. All these expectations can be explored by the current worm-type algorithm, and remain to be a future work.

The efficiency of the current worm algorithm implies its broad applications in a variety of spin and hard-core systems. A straightforward application is to simulate the QTFI on other lattices regardless of dimensionality. For the high dimension $d \geq 3$, one expects very minor or absent critical slowing down, and thus interesting logarithmic corrections can be examined. It can be also of significant relevance in solid-state experiments since the pairing terms $\sigma_i^+ \sigma_j^+$ and $\sigma_i^- \sigma_j^-$ are found to occur in frustrated quantum materials due to the dipolar-octupolar doublets [46–60]. Further, in addition to the external field h , one can introduce pairing interaction $\sigma_i^z \sigma_j^z$ along the σ^z direction, which can be either ferromagnetic or antiferromagnetic. This allows the worm-type study of quantum spin systems with geometric frustration with respect to the σ^z component. In combination with the so-called clock Monte Carlo method [61], one can even study spin systems with long-range $\sigma_i^z \sigma_j^z$ interaction without heavy computational overhead. Finally, we mention that a similar worm algorithm has recently been used in the SSE representation of the hard-core bosonic Hubbard model with pairing terms [62].

ACKNOWLEDGMENTS

We acknowledge N. Prokofiev for initializing the project and X.-P. Yao for technical help in preparing Fig. 1(c). This work is supported by the National Natural Science Foundation of China under Grant No. 11625522.

- [1] Sachdev Subir, *Quantum Phase Transitions* (Cambridge University Press, Cambridge, 2011).
- [2] A. Dutta, G. Aeppli, B. K. Chakrabarti, U. Divakaran, T. F. Rosenbaum, and D. Sen, *Quantum Phase Transitions in Transverse Field Spin Models: From Statistical Physics to Quantum Information* (Cambridge University Press, 2015).
- [3] P. Pfeuty, One-dimensional ising model with a transverse field, *Ann. Phys. (NY)* **57**, 79 (1970).

- [4] G. Vidal, Classical Simulation of Infinite-Size Quantum Lattice Systems in One Spatial Dimension, *Phys. Rev. Lett.* **98**, 070201 (2007).
- [5] H. W. J. Blöte and Y. Deng, Cluster monte carlo simulation of the transverse ising model, *Phys. Rev. E* **66**, 066110 (2002).
- [6] A. Kitaev and J. Preskill, Topological Entanglement Entropy, *Phys. Rev. Lett.* **96**, 110404 (2006).

- [7] M. Levin and X.-G. Wen, Detecting Topological Order in A Ground State Wave Function, *Phys. Rev. Lett.* **96**, 110405 (2006).
- [8] A. F. Albuquerque, F. Alet, C. Sire, and S. Capponi, Quantum critical scaling of fidelity susceptibility, *Phys. Rev. B* **81**, 064418 (2010).
- [9] T. Kaya, One-dimensional quantum transverse-field ising model: A semiclassical transfer matrix approach, *Int. J. Mod. Phys. B* **24**, 5457 (2010).
- [10] O. F. Syljuåsen and A. W. Sandvik, Quantum monte carlo with directed loops, *Phys. Rev. E* **66**, 046701 (2002).
- [11] H. Rieger and N. Kawashima, Application of a continuous time cluster algorithm to the two-dimensional random quantum ising ferromagnet, *Eur. Phys. J. B* **9**, 233 (1999).
- [12] N. V. Prokof'ev, B. V. Svistunov, and I. S. Tupitsyn, "Worm" algorithm in quantum Monte Carlo simulations, *Phys. Lett. A* **238**, 253 (1998).
- [13] T. Ikegami, S. Miyashita, and H. Rieger, Griffiths-mccoy singularities in the transverse field ising model on the randomly diluted square lattice, *J. Phys. Soc. Jpn.* **67**, 2671 (1998).
- [14] S. V. Isakov and R. Moessner, Interplay of quantum and thermal fluctuations in a frustrated magnet, *Phys. Rev. B* **68**, 104409 (2003).
- [15] V. I. Iglovikov, R. T. Scalettar, R. R. P. Singh, and J. Oitmaa, Disorder line and incommensurate floating phases in the quantum ising model on an anisotropic triangular lattice, *Phys. Rev. B* **87**, 214415 (2013).
- [16] Z. Y. Xie, J. Chen, M. P. Qin, J. W. Zhu, L. P. Yang, and T. Xiang, Coarse-graining renormalization by higher-order singular value decomposition, *Phys. Rev. B* **86**, 045139 (2012).
- [17] S. R. White, Density Matrix Formulation for Quantum Renormalization Groups, *Phys. Rev. Lett.* **69**, 2863 (1992); Density-Matrix Algorithms for Quantum Renormalization Groups, *Phys. Rev. B* **48**, 10345 (1993).
- [18] F. Verstraete and J. I. Cirac, Renormalization algorithms for quantum-many body systems in two and higher dimensions, *arXiv:cond-mat/0407066*.
- [19] G. Carleo and M. Troyer, Solving the quantum many-body problem with artificial neural networks, *Science* **355**, 602 (2017).
- [20] J. Carrasquilla and R. G. Melko, Machine learning phases of matter, *Nat. Phys.* **13**, 431 (2017).
- [21] N. Prokof'ev and B. Svistunov, Worm Algorithms for Classical Statistical Models, *Phys. Rev. Lett.* **87**, 160601 (2001).
- [22] Y. Deng, T. M. Garoni, and A. D. Sokal, Dynamic Critical Behavior of the Worm Algorithm for the Ising Model, *Phys. Rev. Lett.* **99**, 110601 (2007).
- [23] Under this condition, τ_a is almost constant for different βL^d . Besides, the acceptance ratio will not be too small or too large.
- [24] M. E. J. Newman and R. M. Ziff, Efficient Monte Carlo Algorithm and High-Precision Results for Percolation, *Phys. Rev. Lett.* **85**, 4104 (2000).
- [25] P. H. L. Martins and J. A. Plascak, Percolation on two- and three-dimensional lattices, *Phys. Rev. E* **67**, 046119 (2003).
- [26] X. Feng, Y. Deng, and H. W. J. Blöte, Percolation transitions in two dimensions, *Phys. Rev. E* **78**, 031136 (2008).
- [27] J. Wang, Z. Zhou, W. Zhang, T. M. Garoni, and Y. Deng, Bond and site percolation in three dimensions, *Phys. Rev. E* **87**, 052107 (2013).
- [28] P. Hou, S. Fang, J. Wang, H. Hu, and Y. Deng, Geometric properties of the fortuin-kasteleyn representation of the ising model, *Phys. Rev. E* **99**, 042150 (2019).
- [29] D. P. Landau and K. Binder, *A Guide to Monte Carlo Simulations in Statistical Physics*, 4th. ed. (Cambridge University Press, Cambridge, 2014), Chap. 7.
- [30] Y. Deng and H. W. J. Blöte, Simultaneous analysis of several models in the three-dimensional ising universality class, *Phys. Rev. E* **68**, 036125 (2003).
- [31] R. Orus and G. Vidal, Simulation of two-dimensional quantum systems on an infinite lattice revisited: Corner transfer matrix for tensor contraction, *Phys. Rev. B* **80**, 094403 (2009).
- [32] G. Evenbly and G. Vidal, Entanglement Renormalization in Two Spatial Dimensions, *Phys. Rev. Lett.* **102**, 180406 (2009).
- [33] R. Orus, Exploring corner transfer matrices and corner tensors for the classical simulation of quantum lattice systems, *Phys. Rev. B* **85**, 205117 (2012).
- [34] E. M. Elçi, J. Grimm, L. Ding, A. Nasrawi, T. M. Garoni, and Y. Deng, Lifted worm algorithm for the ising model, *Phys. Rev. E* **97**, 042126 (2018).
- [35] K. Binder, "Clusters" in the ising model, metastable states and essential singularity, *Ann. Phys. (NY)* **98**, 390 (1976).
- [36] M. E. Fisher, The theory of condensation and the critical point, *Phys. Phys. Fiz.* **3**, 255 (1967).
- [37] Q. Liu, Y. Deng, and T. M. Garoni, Worm monte carlo study of the honeycomb-lattice loop model, *Nucl. Phys. B* **846**, 283 (2011).
- [38] H. Saleur and B. Duplantier, Exact Determination of the Percolation Hull Exponent in Two Dimensions, *Phys. Rev. Lett.* **58**, 2325 (1987).
- [39] A. Coniglio, Fractal Structure of Ising and Potts Clusters: Exact Results, *Phys. Rev. Lett.* **62**, 3054 (1989).
- [40] Q. Liu, Y. Deng, T. M. Garoni, and H. W. J. Blöte, The o(n) loop model on a three-dimensional lattice, *Nucl. Phys. B* **859**, 107 (2012).
- [41] M. Nielsen and I. Chuang, *Quantum Computation and Quantum Information* (Cambridge University Press, Cambridge, 2010).
- [42] P. Zanardi and N. Paunković, Ground state overlap and quantum phase transitions, *Phys. Rev. E* **74**, 031123 (2006).
- [43] L. Wang, Y.-H. Liu, J. Imriška, P. N. Ma, and M. Troyer, Fidelity Susceptibility Made Simple: A Unified Quantum Monte Carlo Approach, *Phys. Rev. X* **5**, 031007 (2015).
- [44] S.-J. Gu and H.-Q. Lin, Scaling dimension of fidelity susceptibility in quantum phase transitions, *Europhys. Lett.* **87**, 10003 (2009).
- [45] L. Campos Venuti and P. Zanardi, Quantum Critical Scaling of the Geometric Tensors, *Phys. Rev. Lett.* **99**, 095701 (2007).
- [46] Y.-P. Huang, G. Chen, and M. Hermele, Quantum Spin Ices and Topological Phases from Dipolar-Octupolar Doublets on the Pyrochlore Lattice, *Phys. Rev. Lett.* **112**, 167203 (2014).
- [47] M. C. Hatnean, M. R. Lees, O. A. Petrenko, D. S. Keeble, G. Balakrishnan, M. J. Gutmann, V. V. Klekovkina, and B. Z. Malkin, Structural and magnetic investigations of single-crystalline neodymium zirconate pyrochlore $\text{Nd}_2\text{Zr}_2\text{O}_7$, *Phys. Rev. B* **91**, 174416 (2015).
- [48] A. Bertin, P. Dalmas de Réotier, B. Fåk, C. Marin, A. Yaouanc, A. Forget, D. Sheptyakov, B. Frick, C. Ritter, A. Amato, C. Baines, and P. J. C. King, $\text{Nd}_2\text{Sn}_2\text{O}_7$: An all-in-all-out pyrochlore magnet with no divergence-free field and anomalously

- slow paramagnetic spin dynamics, *Phys. Rev. B* **92**, 144423 (2015).
- [49] E. Lhotel, S. Petit, S. Guitteny, O. Florea, M. Ciomaga Hatnean, C. Colin, E. Ressouche, M. R. Lees, and G. Balakrishnan, Fluctuations and All-in–All-Out Ordering in Dipole-Octupole $\text{Nd}_2\text{Zr}_2\text{O}_7$, *Phys. Rev. Lett.* **115**, 197202 (2015).
- [50] J. Xu, V. K. Anand, A. K. Bera, M. Frontzek, D. L. Abernathy, N. Casati, K. Siemensmeyer, and B. Lake, Magnetic structure and crystal-field states of the pyrochlore antiferromagnet $\text{Nd}_2\text{Zr}_2\text{O}_7$, *Phys. Rev. B* **92**, 224430 (2015).
- [51] V. K. Anand, A. K. Bera, J. Xu, T. Herrmannsdörfer, C. Ritter, and B. Lake, Observation of long-range magnetic ordering in pyrochlore $\text{Nd}_2\text{Hf}_2\text{O}_7$: A neutron diffraction study, *Phys. Rev. B* **92**, 184418 (2015).
- [52] O. Benton, Quantum origins of moment fragmentation in $\text{Nd}_2\text{Zr}_2\text{O}_7$, *Phys. Rev. B* **94**, 104430 (2016).
- [53] J. Xu, C. Balz, C. Baines, H. Luetkens, and B. Lake, Spin dynamics of the ordered dipolar-octupolar pseudospin- $\frac{1}{2}$ pyrochlore $\text{Nd}_2\text{Zr}_2\text{O}_7$ probed by muon spin relaxation, *Phys. Rev. B* **94**, 064425 (2016).
- [54] V. K. Anand, D. L. Abernathy, D. T. Adroja, A. D. Hillier, P. K. Biswas, and B. Lake, Muon spin relaxation and inelastic neutron scattering investigations of the all-in/all-out antiferromagnet $\text{Nd}_2\text{Hf}_2\text{O}_7$, *Phys. Rev. B* **95**, 224420 (2017).
- [55] P. Dalmas de Réotier, A. Yaouanc, A. Maisuradze, A. Bertin, P. J. Baker, A. D. Hillier, and A. Forget, Slow spin tunneling in the paramagnetic phase of the pyrochlore $\text{Nd}_2\text{Zr}_2\text{O}_7$, *Phys. Rev. B* **95**, 134420 (2017).
- [56] R. Sibille, E. Lhotel, V. Pomjakushin, C. Baines, T. Fennell, and M. Kenzelmann, Candidate Quantum Spin Liquid in the Ce^{3+} Pyrochlore Stannate $\text{Ce}_2\text{Sn}_2\text{O}_7$, *Phys. Rev. Lett.* **115**, 097202 (2015).
- [57] Y.-D. Li and G. Chen, Symmetry enriched $U(1)$ topological orders for dipole-octupole doublets on a pyrochlore lattice, *Phys. Rev. B* **95**, 041106(R) (2017).
- [58] J. Gaudet, E. M. Smith, J. Dudemaine, J. Beare, C. R. C. Buhariwalla, N. P. Butch, M. B. Stone, A. I. Kolesnikov, G. Xu, D. R. Yahne, K. A. Ross, C. A. Marjerrison, J. D. Garrett, G. M. Luke, A. D. Bianchi, and B. D. Gaulin, Quantum Spin Ice Dynamics in the Dipole-Octupole Pyrochlore Magnet $\text{Ce}_2\text{Zr}_2\text{O}_7$, *Phys. Rev. Lett.* **122**, 187201 (2019).
- [59] B. Gao, T. Chen, D. W. Tam, C.-L. Huang, K. Sasmal, D. T. Adroja, F. Ye, H. Cao, G. Sala, M. B. Stone, C. Baines, J. A. T. Verezhak, H. Hu, J.-H. Chung, X. Xu, S.-W. Cheong, M. Nallaiyan, S. Spagna, M. Brian Maple, A. H. Nevidomskyy *et al.*, Experimental signatures of a three-dimensional quantum spin liquid in effective spin-1/2 $\text{Ce}_2\text{Zr}_2\text{O}_7$ pyrochlore, *Nat. Phys.* **15**, 1052 (2019).
- [60] Y. D. Li and G. Chen, Non-spin-ice pyrochlore $U(1)$ quantum spin liquid: Manifesting mixed symmetry enrichments, *Phys. Rev. Research* **2**, 013334 (2020).
- [61] M. Michel, X. Tan, and Y. Deng, Clock Monte Carlo methods, *Phys. Rev. E* **99**, 010105(R) (2019).
- [62] A. J. R. Heng, W. Guo, A. W. Sandvik, and P. Sengupta, Pair hopping in systems of strongly interacting hard-core bosons, *Phys. Rev. B* **100**, 104433 (2019).